

ALMA OBSERVATIONS OF W HYA: IMPACT OF MISSING BASELINES

DO THI HOAI, PHAM TUAN ANH, PHAM TUYET NHUNG, PIERRE DARRIULAT, PHAM NGOC DIEP, NGUYEN BICH NGOC, AND TRAN THI THAI

Department of Astrophysics, Vietnam National Space Center, Vietnam Academy of Science and Technology, 18, Hoang Quoc Viet, Nghia Do, Cau Giay, Ha Noi, Vietnam. dthoai@vnsc.org.vn, ptanh@vnsc.org.vn

Received August xx, 2021; accepted xx xx, 2021

Abstract: The lack of short baselines, referred to as short-spacing problem (SSP), is a well-known limitation of the performance of radio interferometers, causing a reduction of the detected flux from large scale source structures. The very large number of antennas operated in the Atacama Large Millimeter/submillimeter Array (ALMA) generates situations for which the impact of the SSP takes a complex form, not simply measurable by a single number, such as the maximal recoverable scale. In particular extended antenna configurations, complemented by a small group of closeby antennas at the centre of the array, may result in a double-humped baseline distribution with a significant gap between the two groups. In such cases one should adopt as effective maximal recoverable scale that associated with the extended array and use only the central array to recover missing flux, as one would do with single dish or ACA (Atacama Compact Array) observations. The impact of the missing baselines can be very important and may easily be underestimated, or even overlooked. The present study uses ALMA archival data of the $^{29}\text{SiO}(8-7)$ line emission of AGB star W Hya as an illustration. A critical discussion of the reliability of the observations away from the star is presented together with comments of a broader scope. Properties of the circumstellar envelope of W Hya within ~ 15 au from the star, many of which are not mentioned in the published literature, are briefly described and compared with R Dor, an AGB star having properties very similar to W Hya.

Key words: stars: AGB and post-AGB – circumstellar matter – stars: individual: W Hya – radio lines: stars – techniques: image processing, interferometric

1. INTRODUCTION

In the recent years, the operation of the Atacama Large Millimeter/submillimeter Array (ALMA) has opened a new era of radio interferometry with an unprecedented number of antennas, offering a broad choice of possible configurations. In particular, the availability of long baselines has often favoured high angular resolution configurations at the detriment of short baselines, resulting in significant losses of detected flux from large source structures. This so-called short-spacing problem (SSP) is well known and has been the subject of numerous studies (Faridani et al. 2018; Braun & Walterbos 1985). In particular, incomplete coverage of the uv plane is known to produce artefacts known as “ghosts” or “invisible distributions” (Chandra et al. 2012, and references therein). The SSP is typically coped with by merging the array data with single dish observations, or, in the case of ALMA, with data collected using the compact array (ACA). However, the high diversity of possible antenna configurations producing short baselines may result in a complex morphology of the map of the array acceptance, the precise knowledge of which is mandatory for a reliable interpretation of the data. In particular, it may not be reducible to a single number, the so-called maximal recoverable scale. In principle, ALMA users are properly warned of this fact and are en-

couraged to produce simulations of the imaging process for the specific antenna configuration being used (see for example Chapter 7 of the ALMA technical handbook¹). In practice, however, it is often easy to underestimate the importance of this measure and the danger to overlook significant imaging distortions is real. We illustrate the argument using archival ALMA observations of the emission of the $^{29}\text{SiO}(\nu=0, J=8-7)$ line by the circumstellar envelope (CSE) of W Hya, an oxygen-rich AGB star at a distance of only $\sim 104_{-11}^{+14}$ pc to the Sun (van Leeuwen 2007). It is a semi-regular variable with a period of ~ 361 days (Samus et al. 2017), often quoted as a Mira (Lebzelter et al. 2005) belonging to spectral class M7.5e-M9ep. Its mass-loss rate is $\sim 10^{-7} M_{\odot}\text{yr}^{-1}$ (Maercker et al. 2008; Khouri et al. 2014a). Its main sequence mass was between 1 and 1.5 M_{\odot} (Khouri et al. 2014b; Danilovich et al. 2017).

2. OBSERVATIONS, DATA REDUCTION AND IMAGING

The present work uses archival observations of W Hya from project ADS/JAO.ALMA#2015.1.01446.S (PI: A. Takigawa), which were carried out for a total of ~ 2 hours on source over three separate blocks between 30 November and 5 December 2015 with ALMA in Cycle 3. In the present work we use mostly blocks 1 and 2, the data of block 3 being of lesser quality, but we

CORRESPONDING AUTHOR: D.T. Hoai and P. Tuan-Anh

¹<https://almascience.nao.ac.jp/documents-and-tools/cycle7/alma-technical-handbook>

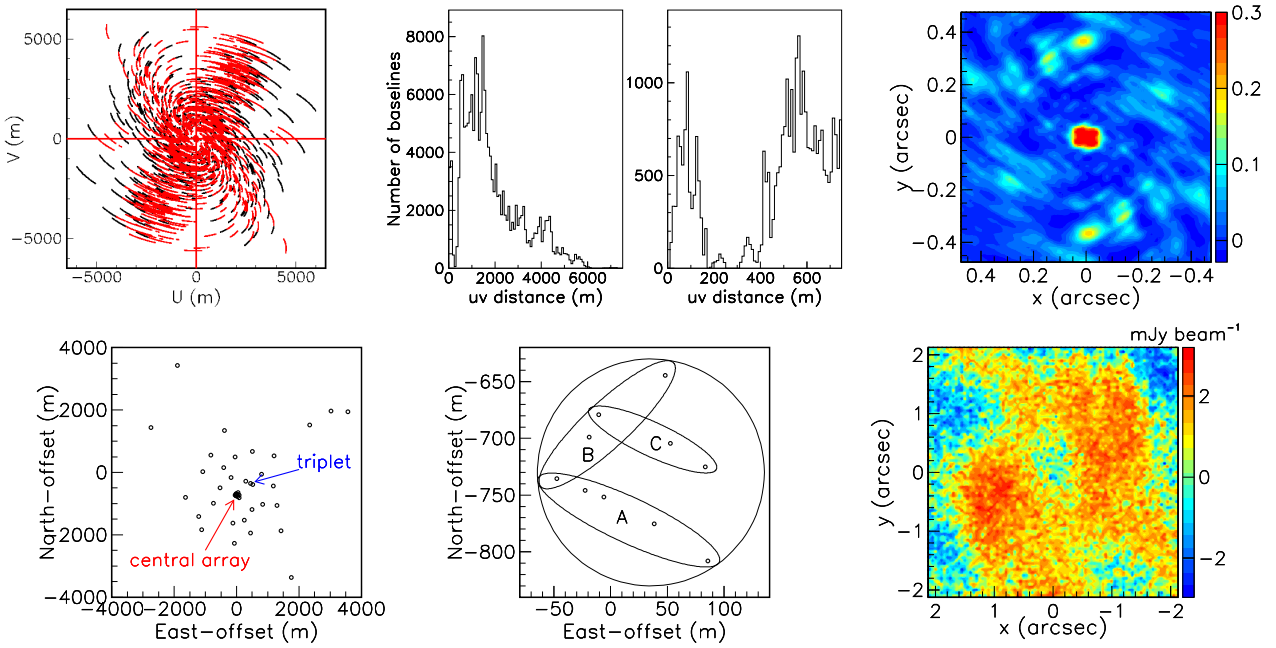


Figure 1. Upper panels: uv coverage for blocks 1+2. In the left panel, block1 is black and block 2 is red. Baseline distributions are shown in the central panels, the rightmost being a zoom on smaller baselines with a bin size of 10 m instead of 80 m. Right: Dirty beam (natural weighting); the colour map is saturated at 0.3 (rather than 1) to show the side lobe of the dirty beam. Lower panels: antenna configuration for blocks 1+2 (42 antennas); the central panel is a zoom on the central array; the red arrow (left) points to the central array, the blue arrow points to a triplet of antennas of the extended array producing short baselines; the circle (centre) has a radius of 100 m; the ellipses define three antenna alignments: A, B and C that are referred to in Figure 7. Right: map of residuals (natural weighting) of a frequency channel close to systemic velocity; the maximum of the colour scale is ~ 3 mJy beam⁻¹, 1.4 times the $1\text{-}\sigma$ level of the noise (2.1 mJy beam⁻¹).

have checked that all the arguments made in the article are independent of the blocks being used, 1+2+3 or 1+2 or 2 alone, each block displaying very similar antenna configurations. The antennas, respectively 33, 41 and 31 in number, were configured in such a way that the baseline lengths were distributed in two groups, one covering between ~ 15 m and ~ 200 m, the other between ~ 400 m and ~ 8 km; the former group included 10 antennas in a circle of 100 m radius (Figure 1). The emission of the ^{29}SiO (8-7) line, with a frequency of 342.9808 GHz (wavelength $\lambda=0.875$ mm), was covered with a frequency resolution of ~ 977 kHz channel^{-1} , corresponding to a channel spacing of 0.854 km s^{-1} . The data have been reduced using standard scripts without continuum subtraction, with particular attention to the scale over which the flux is reliably recoverable. Both imaging codes CASA and GILDAS have been used². We have checked the consistency between the results obtained with the two codes and with different parameters of the deconvolution algorithms, including weights, masks, number of iterations, etc. In all cases, a proper behaviour was observed and the arguments developed in the article were found to be valid independently from these. As an illustration, we show in Figure 1 the dirty beam and a map of residuals obtained with GILDAS using natural weighting. Imaging produces a beam of 63×52 mas² with PA=79° with natural weighting and a beam of 52×38 mas² with PA=99° with robust weighting (threshold of 1).

Maps of the continuum emission are shown in Figure 2. After beam deconvolution, Gaussian fits to the stellar disc give a diameter of 35 ± 2 mas FWHM, in good agreement with earlier evaluations (Vlemmings et al. 2019). We use coordinates centred on the continuum emission, x pointing east, y pointing north and z pointing away from Earth. The projected distance to the star is calculated as $R = \sqrt{x^2 + y^2}$. Position angles, ω , are measured counter-clockwise from north. The Doppler velocity V_z spectrum is centred on a systemic velocity of 40.4 km s^{-1} .

Figure 3 displays the brightness distribution of the ^{29}SiO (8-7) emission in a $R < 2$ arcsec circle centred at the origin; a Gaussian fit to the noise gives a σ of 2.1 mJy beam⁻¹. Also shown are the Doppler velocity spectrum and the intensity map multiplied by R , the latter displaying a complex pattern that is further illustrated in Figure 4, using polar rather than Cartesian sky coordinates. The observed pattern shows back-to-back outflows and a depression around $R \sim 0.45$ arcsec, deeper when using natural weighting than when using robust weighting. Overall, it suggests successive emission in a plane close to the plane of the sky, at intervals of typically 0.25 arcsec, meaning some 30 years for a projected expansion velocity of 4 km s^{-1} (see Section 4), of three successive pairs of back-to-back outflows differently oriented on the plane. Such a pattern has never been observed in earlier studies of AGB stars; we show in the next section that it is an artefact of the particular

antenna configuration.

3. IMPACT OF THE TWO-HUMPED BASELINE DISTRIBUTION

3.1. General considerations

Before addressing the specific case of the present W Hya observations, we briefly recall some basic features of radio interferometry. The complex visibility distribution in the uv plane, $V(u, v)$, is defined as the Fourier transform of the source brightness distribution in the sky plane, $I(x, y)$:

$$\begin{aligned} V(u, v) &= \int I(x, y) e^{-2i\pi(ux+vy)} dx dy \\ I(x, y) &= \int V(u, v) e^{2i\pi(ux+vy)} du dv \end{aligned}$$

A specific antenna configuration, operated for a given period of Earth rotation, samples only part of the complex visibility distribution in the uv plane, defined by a sampling function $S(u, v)$, a sum of two-dimensional delta-functions. The Fourier transform of the measured visibilities, $I_D(x, y)$, called “dirty map”, is the convolution of the source brightness distribution by the Fourier transform of the sampling function, $B(x, y)$, called Point Spread Function or “dirty beam”:

$$\begin{aligned} I_D(x, y) &= \int S(u, v) V(u, v) e^{2i\pi(ux+vy)} du dv \\ &= \int B(x - x', y - y') I(x', y') dx' dy' \end{aligned}$$

Accordingly, extended distributions of baseline lengths produce high angular resolutions, the higher the longer the longest baselines. Conversely, the shortest baselines define the maximal recoverable scale beyond which flux fails to be detected. The definition of the shortest and longest baselines is somewhat arbitrary, depending on how progressively the baseline length distribution rises and falls; moreover, it assumes a reasonably smooth baseline distribution: the presence of peaks and/or gaps impacts the dirty map in a complex way that cannot be summarised by single numbers such as angular resolution and maximal recoverable scale.

Quantitatively, a source brightness distribution $I'(x, y) = k^2 I(kx, ky)$, obtained by shrinking $I(x, y)$ by a factor k in the plane of the sky, produces a visibility distribution in the uv plane expanded by the same factor k :

$$\begin{aligned} V'(u, v) &= k^2 \int I(kx, ky) e^{-2i\pi(ux+vy)} dx dy \\ &= \int I(x', y') e^{-2i\pi[(u/k)x' + (v/k)y']} dx' dy' \\ &= V(u/k, v/k) \end{aligned}$$

Similarly, an antenna pattern obtained by shrinking the pattern described by the sampling function $S(u, v)$, itself described by a sampling function

²<https://casa.nrao.edu> and <https://imager.oas.u-bordeaux.fr/>

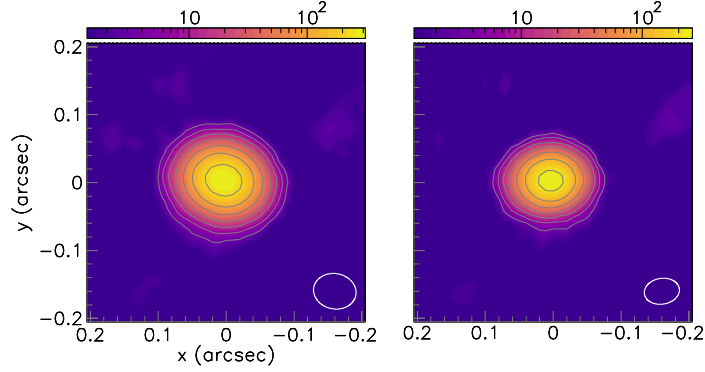


Figure 2. Maps of the continuum brightness obtained with natural (left) and robust (right) weighting. The colour scale is in units of mJy beam^{-1} . The beam is shown in the lower right corner of each panel.

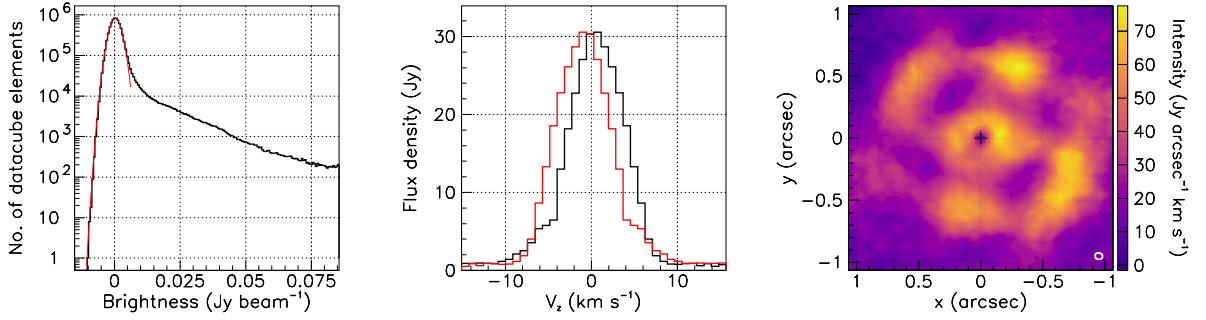


Figure 3. Left: brightness distribution in a $R < 2$ arcsec circle (natural weighting); the red line shows the result of a Gaussian fit. Middle: Doppler velocity spectrum integrated over $R < 1$ arcsec; the asymmetry, illustrated by the mirror spectrum shown in red, is the result of the absorption centred at the terminal wind velocity of $\sim -5.5 \text{ km s}^{-1}$ (see Figure 9). Right: map of the intensity integrated over $|V_z| < 8 \text{ km s}^{-1}$ and multiplied by R . The beam is shown in the lower right corner.

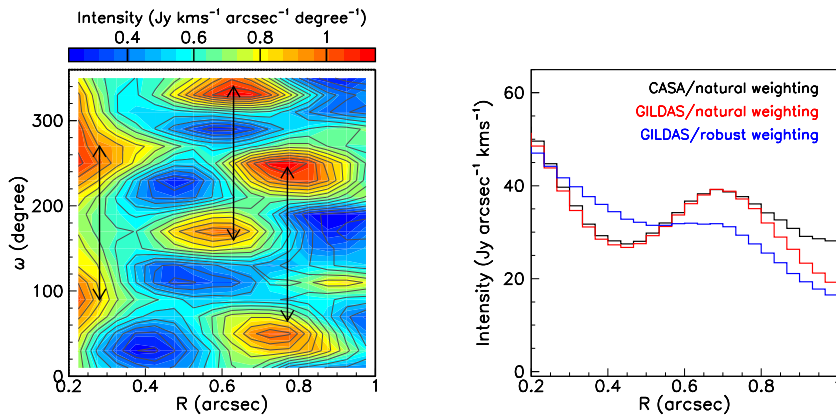


Figure 4. Comparison between the clean maps (integrated over $|V_z| < 5 \text{ km s}^{-1}$) obtained using different deconvolution algorithms. Left: clean map in the ω vs R plane reconstructed using CASA (colour) and using GILDAS (contours). The arrows show a spacing of 180° in position angle. Right: R distributions integrated over position angle.

$S'(u, v) = k^2 S(ku, kv)$, produces a dirty map:

$$\begin{aligned} I'_D(x, y) &= k^2 \int S(ku, kv) V(u, v) e^{2i\pi(ux+vy)} du dv \\ &= \int S(u', v') V(u'/k, v'/k) e^{2i\pi[u'(x/k)+v'(y/k)]} du' dv' \\ &= \int S(u', v') V'(u', v') e^{2i\pi[u'(x/k)+v'(y/k)]} du' dv' \end{aligned}$$

Namely, the dirty map produced by an antenna pattern shrunk by a factor k is the same as the dirty map obtained by expanding by a factor k the dirty map of the source shrunk by the same factor k . Whatever visibility is not sampled by the sampling function does not contribute to the dirty map. Producing a clean map implies therefore assigning values to the complex visibility in the regions of the uv plane that are not sampled by $S(u, v)$. Arbitrary visibilities in such regions have no effect on the dirty map but cause the Fourier transform of the visibility distribution to arbitrarily deviate from the source brightness distribution.

In the present case of a two-humped baseline distribution, we can approach the study of the measurement process from two different points of view. A first approach is to consider the extended array as the basic array and to study the contribution obtained by adding the central array. This is reminiscent of what is commonly done when merging interferometer data with single dish data, or, in the case of ALMA, main 12 m array data with ACA data. A second approach is to consider as basic array an array that would include the complete array, central+extended, as well as additional antennas filling the baseline gap between the two; one would then study the impact of removing these additional antennas and would speak about the effect of “missing baselines”. In the present work, we may take one or the other approach: our ambition is not to produce an exhaustive treatment of the problem but simply to illustrate with a specific example the danger of underestimating its importance and of unduly using concepts such as maximal recoverable scale or angular resolution, which are insufficient to properly describe the reality of the measurement process.

3.2. W Hya observations: radial distributions

In order to evaluate the impact of the two-humped baseline distribution on the results presented in Section 2 and to estimate the projected distance from the star up to which they can be considered reliable, we simulate the response of the array to the emission of an optically thin isotropic wind of constant radial velocity, with an intensity decreasing in inverse proportion to the projected distance to the star, R . To avoid the singularity of such a wind at $R=0$, we use a uniform brightness of $72 \text{ Jy arcsec}^{-2}$ within the disc $R < 0.1 \text{ arcsec}$. As the observed pattern is seen to evolve smoothly from frequency channel to frequency channel, it is sufficient at this stage to ignore the dependence on Doppler velocity. The clean image obtained from the visibilities produced

by the actual antenna configuration is shown in Figure 5 and displays a pattern strikingly similar to that observed for the real data: a same depression around $R \sim 0.45 \text{ arcsec}$ and a same structure in successive pairs of back-to-back outflows. This unexpected result raises two questions: what is precisely causing the effect? And how far away from the star can the wind morphology be reliably evaluated?

The left panel of Figure 6 displays the respective contributions of the central and extended arrays to the radial brightness distribution of the $^{29}\text{SiO}(8-7)$ emission. Cleaning uses natural weighting. The former is seen to probe large distances from the star and the latter short distances. The associated beam sizes (FWHM) are 63×52 , 58×46 and $1100 \times 880 \text{ mas}^2$, for the whole, extended and central arrays, respectively. The middle-left panel shows the same distributions for the isotropic wind model described above. The central array is again seen to probe large distances and the extended array, short distances. In this case we can compare (right panel) the real radial distribution of the source brightness with its image obtained from the whole array: it shows a broad depression at the scale of $\pm 0.2 \text{ arcsec}$, centred at an approximate distance of 0.45 arcsec : the missing baselines between 200 and 400 m are shown to cause an oscillation of the detected brightness about the source brightness with a peak to valley ratio of ~ 2.6 . This oscillation is seen at a similar level on the data (left panel of Figure 6 and Figure 2b of Takigawa et al. 2017), implying that it is an artefact.

In order to shed light on its genesis, we display in the right panel of Figure 6 the radial profiles of the dirty beams associated with the whole and extended arrays, respectively. The profile of the beam of the extended array oscillates beyond the main lobe, the width of which is defined by the longest baselines. Qualitatively, it behaves as an Airy function but the first negative oscillation is deeper; the reason is the missing baselines below some 400 m, associated with a main lobe of width $\sim 1.3 \times \lambda/\text{BL} \sim 0.6 \text{ arcsec}$ (twice the maximal recoverable scale defined in the ALMA technical handbook), which needs to be subtracted from the profile of the dirty beam. The profile of the beam of the whole array is obtained from the profile of the beam of the extended array by adding the contribution of the central array, confined below some 200 m instead of 400 m, namely associated with a main lobe twice wider than required for a proper uv coverage, $\sim 1.2 \text{ arcsec}$. As a result, the radial profile of the dirty beam stays positive up to nearly 1 arcsec (this was already apparent on its map displayed in the upper-right panel of Figure 1) and the dirty map is inflated in the angular region between the main lobes of a 400 m and a 200 m baseline distributions, namely between $\sim 0.6 \text{ arcsec}$ and $\sim 1.2 \text{ arcsec}$. The cleaning process reduces this excess to an oscillation about the source brightness.

None of the numbers quoted in this discussion is precisely defined: the fall of the baseline distribution of the central array covers between 100 and 200 m while the rise of the baseline distribution of the extended ar-

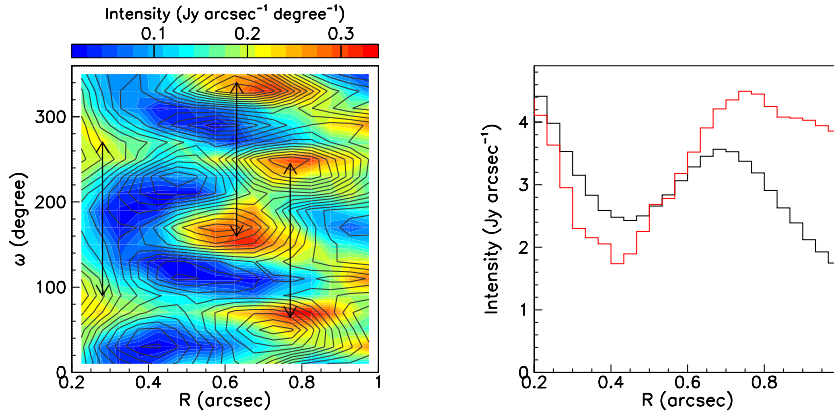


Figure 5. Imaging the isotropic wind model of emission with the antenna configuration of data sets 1 and 2. Left: clean map (ω vs R) of the model intensity, contours are from the data. Right: R distributions (red is for the model, black is for the data). The data are averaged over $|V_z| < 5 \text{ km s}^{-1}$.

ray covers between 400 m and 500 m.

A consequence of the results displayed in Figure 6 is that the brightness detected at projected distances from the star in excess of some 0.2 arcsec is obtained exclusively from the central array. The contribution of the extended array is confined to short distances from the star, the maximal recoverable scale (as defined in the ALMA technical handbook) associated with a 400 m minimal baseline being only $0.6 \times \lambda / \text{BL} = 0.27$ arcsec: the role of the extended array is to provide a high angular resolution at short distances from the star. Note that using robust weighting rather than natural weighting gives a stronger weight to the extended array in comparison with the central array: as a result, as shown in Figure 4, the depression is attenuated and less missing flux is recovered at large projected distances from the star.

3.3. W Hya observations: production of artefacts

The arguments developed in the preceding sub-section have clarified the role of the missing baselines in producing a depression of the radial distribution of the detected brightness covering projected distances from the star between approximately 0.2 and 0.6 arcsec. They have not addressed the production of artefacts mimicking the emission of back-to-back outflows, evidence for which is given in the left panel of Figure 5, but they have shown that the image obtained at projected distances from the star in excess of ~ 0.2 arcsec is governed by the antenna configuration of the central array. Strong additional evidence is shown in Figure 7 by displaying images obtained with selected subsamples of the antennas of the central array. A particularly spectacular illustration is obtained by disregarding the central array altogether (lower row of the figure). Then short baselines are provided exclusively by the triplet of antennas indicated by a blue arrow in Figure 1. They completely dominate the pattern observed beyond $R \sim 0.2$ arcsec, which is now a set of fringes oriented at position angle 25° modulo 180° and separated by 0.6 arcsec.

While the missing baselines are to be blamed for

the production of the radial depression, the production of artefacts at larger projected distances from the star is therefore to be blamed exclusively on the insufficient uv coverage provided by the central array. A central array offering a better uv coverage would have made it possible to obtain reliable images up to projected distances from the star at arcsec scale. In the present case, however, this is unrealistic. The left and central panels of Figure 8 compare the images of the data and of the model in projection on the sky plane, showing strong similarity between the patterns displayed by the two images: qualitatively, it suggests that the emission of the W Hya CSE is isotropic up to distances of at least 0.5 arcsec from the centre of the star. However, ascertaining such a statement requires new observations providing adequate coverage of the uv plane.

The above discussion shows the importance of ensuring that the detection of back-to-back outflows is not in fact the result of artefacts caused by an improper uv coverage. Such pairs of outflows have been observed earlier in the CSEs of several AGB stars, such as R Dor (Nhung et al. 2021), EP Aqr (Nhung et al. 2019), RS Cnc (Winters et al. 2021), etc. In all these cases a distinctive feature was the observed asymmetry of the Doppler velocities of the members of the pair. This provides indeed a useful criterion against artefacts, but cannot be used if the outflows are in the plane of the sky. The right panel of Figure 8 displays the V_z vs ω map of the emission of the ^{29}SiO line averaged in the region $0.3 < R < 0.6$ arcsec where the artefacts are apparent. It shows the absence of significant back-to-back asymmetry in V_z . We checked that this result is independent from the specific R interval used to make the comparison. We note the presence of a small blob of enhanced emission centred at $V_z \sim 5.5 \text{ km s}^{-1}$ and $\omega \sim 290^\circ$, which we discuss briefly at the end of the next section.

4. W HYA NEAR THE STELLAR DISC: A COMPARISON WITH R DOR

The arguments developed in the preceding sections have shown that the observed data-cube of $^{29}\text{SiO}(8-7)$ emis-

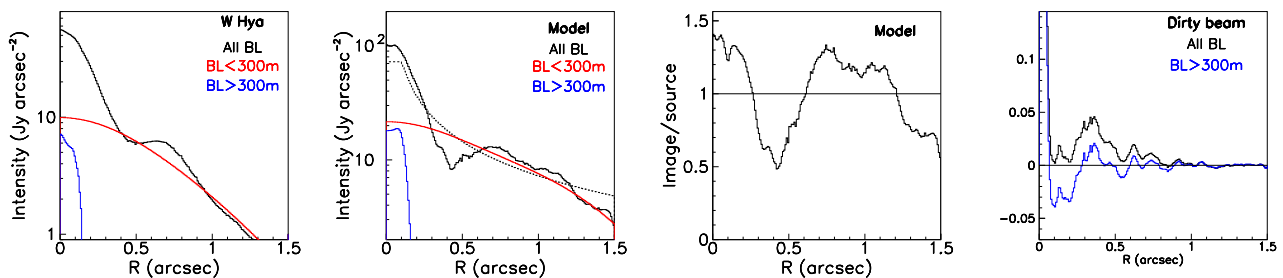


Figure 6. Left and middle-left panels: Radial distributions averaged over position angle obtained from the clean images (natural weighting) when using the whole array (black), the central array (red) or the extended array (blue). The left panel is for the $^{29}\text{SiO}(8-7)$ emission averaged over $|V_z| < 5 \text{ km s}^{-1}$ and the middle-left panel for the isotropic wind model, shown as a dotted line. The separation between central and extended arrays is made by a simple cut at a baseline length of 300 m. We have checked that a same result is obtained by retaining instead the proper antennas. We have checked that a point source (quasar) produces a same flux density in the clean maps associated with each antenna configuration. Middle-right panel: radial dependence of the ratio between the source brightness and its image (natural weighting) for the isotropic wind model. Right panel: radial profiles of the dirty beams (averaged over position angle) of the whole array (black) and the extended array (blue). The main lobe is cut in order to properly show the wings of the profiles.

sion is reliable up to distances of over 15 au (0.15 arcsec) from the star. In this range, W Hya has recently been the object of detailed studies: observations in the visible and near-visible using NACO and SPHERE-ZIMPOL on the VLT and AMBER on the VLTI (Norris et al. 2012; Ohnaka et al. 2016, 2017; Khouri et al. 2020; Hadjara et al. 2019) have given evidence for a clumpy and dusty layer, displaying important variability at short time scale. Dust grains, mostly aluminium composites, are found to have sizes ranging between 0.1 and 0.5 microns. In the near-IR, using MIDI on the VLTI, Zhao-Geisler et al. (2015) have confirmed this result as have Vlemmings et al. (2017, 2019) using ALMA to observe continuum and $\text{CO}(\nu=1, J=3-2)$ emissions close to the star. Khouri et al. (2015) have proposed a simple model that also confirms this result, showing that SiO emits at larger distances. Khouri et al. (2014a,b) have used Herschel in the infrared to measure the $^{12}\text{C}/^{13}\text{C}$ ratio as 18 ± 10 , to detect emission from H_2O and ^{28}SiO and to establish that $\sim 1/3$ of SiO atoms are locked up in dust. Takigawa et al. (2017), in their analysis of the present observations, have shown that while the spatial distribution of AIO molecules is confined within ~ 6 au, ^{29}SiO molecules extend beyond ~ 10 au without significant depletion. Takigawa et al. (2019) argue that transition alumina containing $\sim 10\%$ of Si is the most plausible source of the dust emission from alumina-rich AGB stars. Also using the present observations, Vlemmings et al. (2017) have explored the inner layer of the CSE. The latter two publications, by Takigawa et al. (2017) and Vlemmings et al. (2017), using the present observations, have obtained important results concerning the shock-heated atmosphere of the star and the mechanism governing the formation of dust, respectively. This does not leave much room to extract from the present observations further information of relevance. Yet, a few features that have not been mentioned in the published literature deserve being briefly presented and commented upon, which we

do in the present section. To do so, we use as a guide ALMA observations of the emission by the CSE of R Dor of the same $^{29}\text{SiO}(8-7)$ molecular line as observed in W Hya (Nhung et al. 2021). The motivation for doing so is the similarity between the two stars (same mass loss rate, very similar long periods and spectral types, absence of technetium in their spectra, etc.) which is often used in the published literature as an encouragement for comparing their properties, as is the case in particular in the work of Vlemmings et al. (2017).

Absorption over and well beyond the stellar disc is illustrated in Figure 9 and found to be qualitatively similar to that of R Dor. A narrow absorption peak is seen at $\sim -5.5 \text{ km s}^{-1}$, slightly lower than for R Dor, corresponding to absorption in the outer SiO layer³, which is expected to extend up to some 100 au from the star (Nhung et al. 2021). The continuum levels measured within 12 au, corresponding to a good coverage of the continuum emission, are in excellent agreement with those measured by Vlemmings et al. (2019): 420 and 580 mJy for W Hya and R Dor respectively. The larger beam size (when measured in au) of the W Hya data causes significant smearing of the absorption. Note that the effect of absorption is visible over the whole R range, irrespective of the SSP, which causes distortions of the image brightness but does not create a signal where there is no emission.

Rotation of the R Dor CSE in the vicinity of the star has been studied in detail (Vlemmings et al. 2018; Homan et al. 2018; Nhung et al. 2021) and found to be solid-body-like up to some ~ 6 au from the star, to reach a maximal velocity of $\sim 6 \text{ km s}^{-1}$ at ~ 8 au and then to slow down and cancel beyond 15 au. It is illustrated in Figure 10. Instead, the W Hya observations, albeit being slightly less sensitive to the presence of a possible rotation because of the larger beam size, show

³We learned after submission of the present manuscript of a very recently published paper by Vlemmings et al. (2021) that gives evidence for $\text{CO}(3-2)$ maser emission at the same Doppler velocity, $\sim -5.5 \text{ km s}^{-1}$, as observed here as terminal velocity.

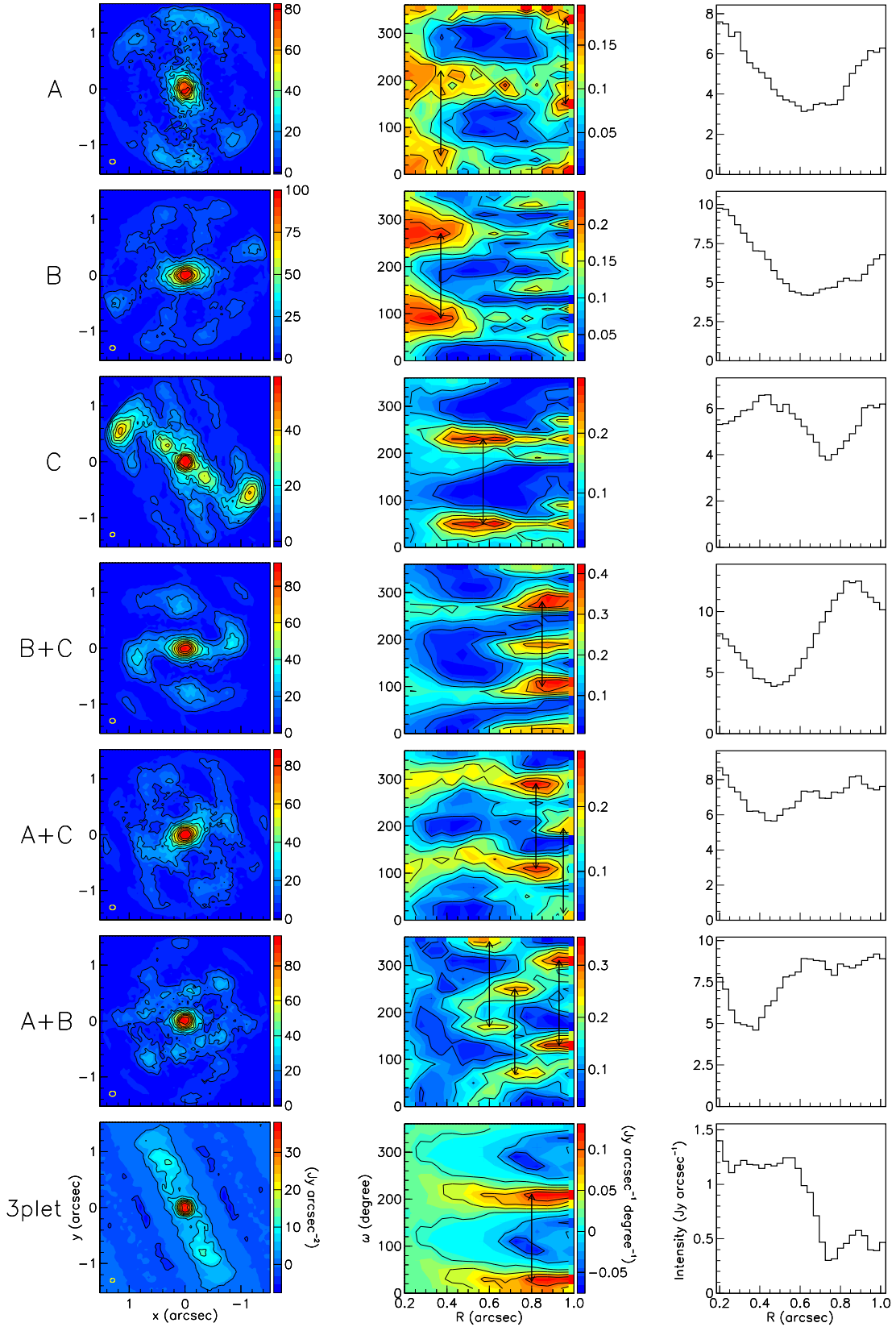


Figure 7. Clean maps of the isotropic wind model emission obtained by using the whole extended array but retaining only a subset of antennas in the central array. Intensity maps are shown on the left column in Cartesian coordinates (y vs x) and in the middle column in polar coordinates (ω vs R); the radial distributions, integrated on position angle, are shown in the right column. From up down, the subsets are A, B, C, B+C, A+C and A+B where A, B and C are defined in the central lower panel of Figure 1. The last row ignores all antennas of the central array, the pattern being exclusively defined by the triplet of antennas indicated by a blue arrow in Figure 1.

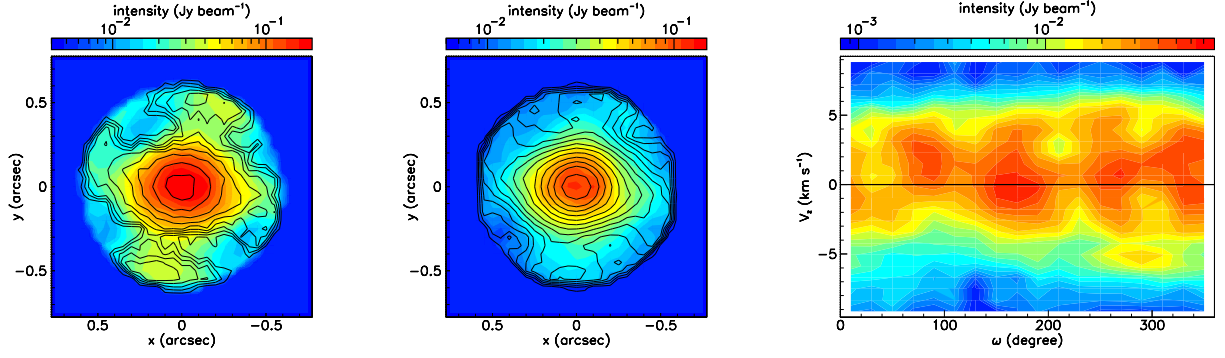


Figure 8. Left and centre: comparison between the intensity map of the ^{29}SiO emission averaged between -4 and 6 km s $^{-1}$ (colour scale) and the model (contours). The left panel uses natural weighting and the central panel uses robust weighting. Both maps are limited to the region $R < 0.6$ arcsec. Right: PV map of the ^{29}SiO emission (V_z vs ω) averaged over the interval $0.3 < R < 0.6$ arcsec.

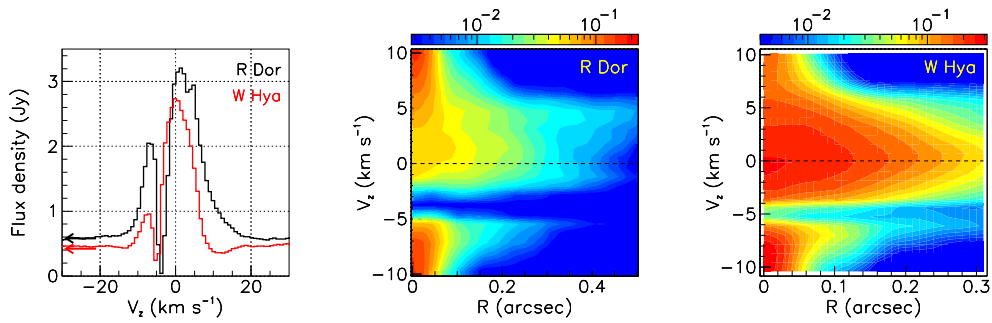


Figure 9. Doppler velocity spectra integrated over $R < 12$ au for R Dor (black) and W Hya (red). The arrows show the continuum levels measured by Vlemmings et al. (2019). Centre and right: PV maps V_z vs R averaged over position angles, for R Dor (centre) and W Hya (right). The colour scales are in units of Jy beam $^{-1}$.

no clear evidence for rotation. From the observed dependence of the mean Doppler velocity on position angle, we infer an upper limit of $\sim 1 \text{ km s}^{-1}$ on a possible rotation velocity averaged between $R=5 \text{ au}$ and $R=10 \text{ au}$ and divided by the sine of the angle between rotation axis and line of sight. In both cases an offset of $\sim 0.5 \text{ km s}^{-1}$ is observed, probably due, at least in part, to absorption. We note that a tilt of 5° of the rotation axis with respect to the line of sight is sufficient to prevent detection of a rotation velocity equal to that at stake in R Dor.

The presence of high Doppler velocity wings in the vicinity of the star has been observed in the CSEs of several oxygen-rich AGB stars and is understood as probing their inner layer where shocks from pulsations and convection cell ejections play an important role. Observations of the $^{29}\text{SiO}(8-7)$ emission from R Dor and W Hya in a ring of radius $5 < R < 10 \text{ au}$ are illustrated in Figure 11. While both stars display high Doppler velocity wings, partly affected by absorption, the effect is less marked in W Hya than in R Dor, with a σ of 4.2 km s^{-1} instead of 5.2 km s^{-1} .

Finally, we note (Figure 12) the presence of a blob of emission in the blue hemisphere, some 10 au north of the star. It has not been mentioned earlier (Takigawa et al. 2017). Such a blob was first observed in R Dor by Decin et al. (2018) and later shown by Nhung et al. (2021) to be caused by a stream of gas rather than by a companion as suggested in earlier analyses (Homan et al. 2018; Decin et al. 2018; Vlemmings et al. 2018). Here, in contrast with R Dor, the distance to the star is independent from Doppler velocity, excluding a sensible interpretation in terms of a gas flow. We show in Figure 13 the ω vs R map integrated over $-11.7 < V_z < -4.8 \text{ km s}^{-1}$ and the Doppler velocity spectrum integrated over the blob, significantly notched by absorption. The present data show that the blob covers essentially a well-defined compact region of the data cube. However, Figure 13 shows the emission trailing $\sim 60^\circ$ west of north toward the region where a blob was observed in the right panel of Figure 8, where imaging is not reliable. Observations using proper uv coverage and possibly including other molecular line emissions would probably help with understanding the nature of the blob.

5. SUMMARY AND CONCLUSIONS

The present work, initiated with the intention of exploring the morpho-kinematics of the CSE of W Hya up to distances at arcsec scale using ALMA observations of the $^{29}\text{SiO}(8-7)$ line, has revealed a major shortcoming preventing such an exploration to be reliably performed.

The lack of uv coverage for baselines between 200 m and 400 m has been found to cause a strong distortion of the radial distribution of the detected flux, with a depression at projected distances centred around 0.45 arcsec ($= \lambda/400 \text{ m}$). As this can easily be overlooked in other observations using antenna configurations with significant intervals of missing baselines, we devoted the major part of the article to a detailed study of the ef-

fect. Antenna configurations combining an extended array with a compact smaller central array are prone to produce baseline distributions made of two families separated by a gap: short baselines not exceeding the diameter of the central array (here $\sim 200 \text{ m}$) and long baselines between either two antennas of the extended array or an antenna of the extended array and one of the central array (here exceeding $\sim 400 \text{ m}$). Beyond the depression, the observed pattern of emission is governed by the detailed configuration of antennas in the central array; as such, if the uv coverage is inadequate, it may take the form of apparent outflows emitted back-to-back. At variance with real back-to-back outflows that are emitted at opposite Doppler velocities these artefacts are independent of the frequency interval being considered, providing a useful discrimination against them. In principle, one should be able to cope with this problem by modelling the morpho-kinematics of the CSE and adjusting the associated parameters to best fit the observed visibilities. In practice, however, the complexity of the physics at stake is such that it would be difficult to obtain a convincingly reliable result: the presence of dust formation, of a complex temperature-dependent gas-dust chemistry and of strong absorption prevent such an enterprise to be credibly successful.

Three earlier publications have been using the same ALMA observations as used in the present article without making explicit reference to the impact of missing baselines. The work of Vlemmings et al. (2017) focuses on the inner part of the CSE, within less than 6 au from the centre of the star, in a region where imaging is perfectly reliable and not at all affected by the missing baselines. Their important conclusions concerning the shock-heated inner atmosphere are therefore fully valid. The work of Takigawa et al. (2017) uses analyses of both AIO and SiO emissions. While the former is confined to the close neighbourhood of the star and is therefore unaffected by the missing baselines, the latter extends further out. Indeed their Figure 2b clearly shows the presence of the depression. However the main conclusion of their work rests on the remark that SiO emission extends much further out than AIO emission. This conclusion not only remains valid but is even strengthened when correcting for the missing flux associated with the missing baselines: their impact is therefore expected to be minimal. Finally, the work of Danilovich et al. (2019), which studies the abundances of sulfur-bearing molecules CS and SiS, extends well beyond the region where imaging is reliable. It is therefore affected by the depression around 0.45 arcsec while these authors state in their article that “W Hya was observed on baselines from 17 m to 11 km , giving sensitivity to angular scales up to about 6 arcsec [...] The full width half maximum of the ALMA primary beam is about 15 arcsec in this frequency range and all of the results presented here are from the inner few arcsec where the reduction in sensitivity is negligible.” It is not up to us to evaluate precisely the impact of the missing baselines on their result. We remark, however, that it is likely not to be very large, being affected only

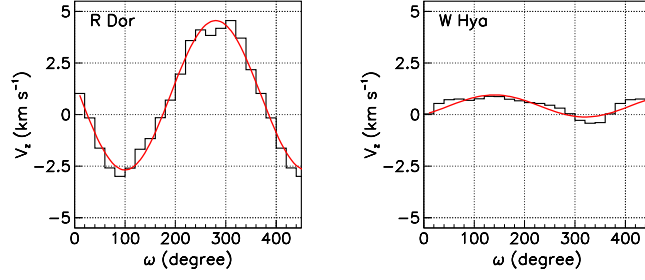


Figure 10. Dependence of $\langle V_z \rangle$ (calculated over $|V_z| < 12 \text{ km s}^{-1}$) on ω for R Dor (left) and W Hya (right) averaged in rings $R=7.5 \pm 3.0 \text{ au}$ and $R=7.5 \pm 2.5 \text{ au}$, respectively. The sine wave fits (km s^{-1}) are $0.5 - 3.6 \sin(\omega - 11^\circ)$ and $0.4 + 0.5 \sin(\omega - 48^\circ)$, respectively.

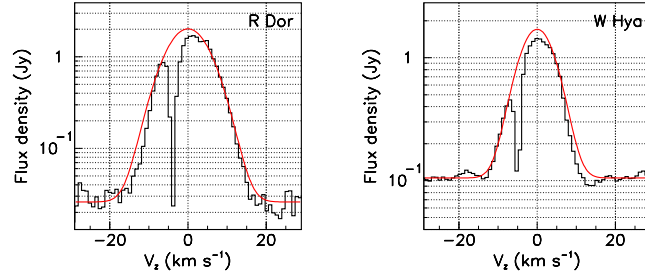


Figure 11. Doppler velocity spectra (black) integrated in a ring of 5 to 10 au centred on R Dor (left) and W Hya (right). Gaussian profiles, superimposed on a constant flux, are shown in red as references. They have σ 's of 5.2 (left) and 4.2 (right) km s^{-1} .

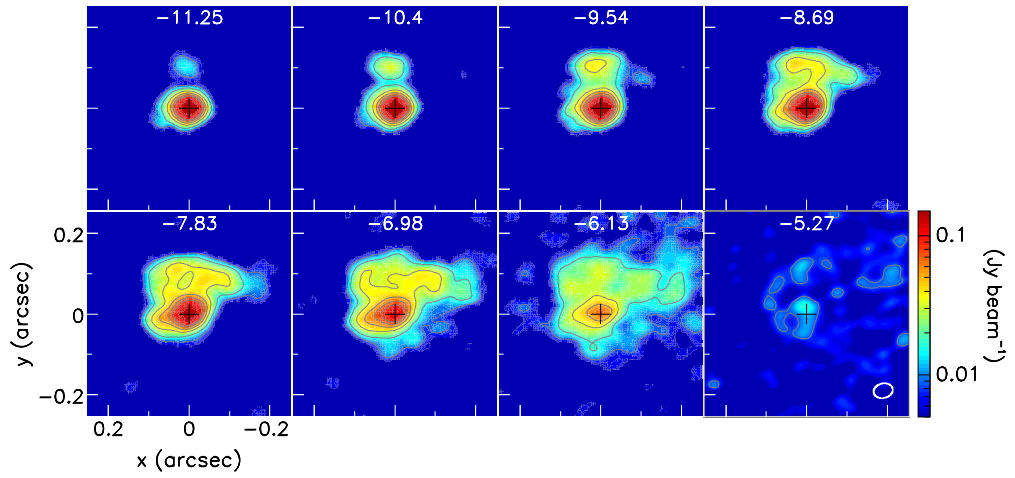


Figure 12. Channel maps of the $^{29}\text{SiO}</math>(8-7) line emission of W Hya in the blue hemisphere showing a blob of enhanced emission. The redmost panel is in the absorption range. Mean Doppler velocities are indicated in each panel. The beam, $52 \times 38 \text{ mas}^2$, $\text{PA}=99^\circ$ (robust weighting), is shown in the lower-right corner of the lower-right panel.$

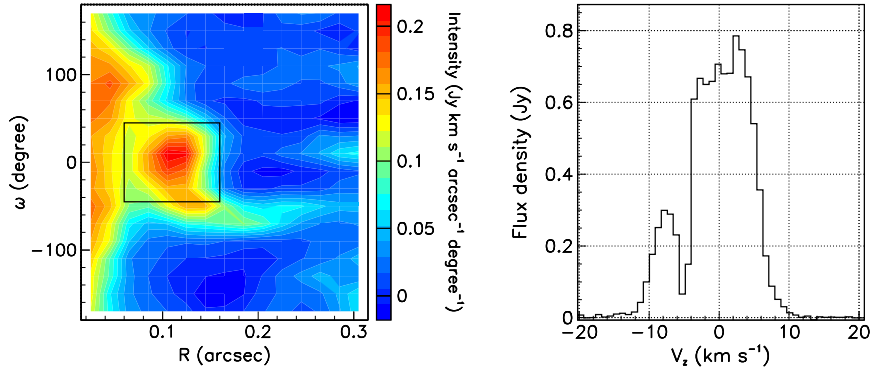


Figure 13. Left: ω vs R map of the $^{29}\text{SiO}(8-7)$ line emission of W Hya integrated over the Doppler velocity interval displayed in Figure 12. Right: Doppler velocity spectrum measured in the rectangle shown in the left panel. The beam is the same as in Figure 12.

by the distortion of the radial distribution.

The impact of the missing baselines would be considerably more severe on studies that rely on the detailed morphology of the image, not simply on the radial distribution of the intensity. It would result in claiming the presence of back-to-back outflows, which would in fact be pure artefacts.

Finally, while being unable to explore reliably the morpho-kinematics of the CSE up to arcsec scale distances, we have mentioned a few features of lesser importance that were not commented upon in the published literature but are significant enough to deserve a brief presentation. They are presented in the form of a comparison with similar features observed in R Dor and include comments on rotation, absorption and broad line widths. Evidence has been given for the presence of a blob of enhanced emission in the blue-shifted hemisphere, some 10 au north of the star, the present data being however insufficient to propose a reliable interpretation.

ACKNOWLEDGEMENTS

We thank Dr. Stéphane Guilloteau for useful discussions and Dr. Aki Takigawa for clarifications on the maximal recoverable scale used in their article. This paper uses ALMA data ADS/JAO.ALMA#2015.1.01446.S. ALMA is a partnership of ESO (representing its member states), NSF (USA) and NINS (Japan), together with NRC (Canada), MOST and ASIAA (Taiwan), and KASI (Republic of Korea), in cooperation with the Republic of Chile. The Joint ALMA Observatory is operated by ESO, AUI/NRAO and NAOJ. The data are retrieved from the JVO/NAOJ portal. We are deeply indebted to the ALMA partnership, whose open access policy means invaluable support and encouragement for Vietnamese astrophysics. Financial support from the World Laboratory, the Odon Vallet Foundation and VNSC is gratefully acknowledged. This research is funded by the Vietnam National Foundation for Science and Technology Development (NAFOSTED) under grant number

103.99-2019.368.

REFERENCES

- Braun R., Walterbos R. A. M., 1985, A solution to the short spacing problem in radio interferometry *A&A*, 143, 307
- Chandra S. S., Svalbe I. D., Guedon J. P., et al., 2012, Recovering missing slices of the discrete Fourier transform using Ghosts, *IEEE Transactions on Image Processing*, 21, 4431
- Danilovich T., Lombaert R., Decin L., et al., 2017, Water isotopologues in the circumstellar envelopes of M-type AGB stars, *A&A*, 602, A14
- Danilovich T., Richards A. M. S., Karakas A. I. et al., 2019, An ALMA view of CS and SiS around oxygen-rich AGB stars, *MNRAS*, 484, 494
- Decin L., Richards A. M. S., Danilovich T. et al., 2018, ALMA spectral line and imaging survey of a low and a high mass-loss rate AGB star between 335 and 362 GHz, *A&A*, 615, A28
- Faridani S., Bigiel F., Flöer L., et al., 2018, A new approach for short-spacing correction of radio interferometric datasets, *Astronomische Nachrichten*, 339, 87
- Hadjara M., Cruzalèbes P., Nitschelm C., et al., 2019, A CO-multilayer outer atmosphere for eight evolved stars revealed with VLTI/AMBER, *MNRAS*, 489, 2595
- Homan W., Danilovich T., Decin L., et al., 2018, ALMA detection of a tentative nearly edge-on rotating disk around the nearby AGB star R Doradus, *A&A*, 614, A113
- Khouri T., de Koter A., Decin, L. et al., 2014a, The wind of W Hydrae as seen by Herschel. I. The CO envelope, *A&A*, 561, A5
- Khouri T., de Koter A., Decin, L. et al., 2014b, The wind of W Hydrae as seen by Herschel. II. The molecular envelope of W Hydrae, *A&A*, 570, A67
- Khouri T., Waters L. B. F. M., de Koter A. et al., 2015, Dusty wind of W Hydrae. Multi-wavelength modelling of the present-day and recent mass loss, *A&A*, 577, A114
- Khouri T., Vlemmings W. H. T., Paladini C. et al., 2020, Inner dusty envelope of the AGB stars W Hydrae, SW Virginis, and R Crateris using SPHERE/ZIMPOL, *A&A*, 635, A200
- Lebzelter T., Hinkle K. H., Wood P. R. et al., 2005, A study of bright Southern long period variables, *A&A*, 431, 623
- Maercker M., Schöier F. L., Olofsson H. et al., 2008, Circumstellar water vapour in M-type AGB stars: radiative

- transfer models, abundances, and predictions for HIFI, *A&A*, 479, 779
- Nhung P. T., Hoai D.T., Tuan-Anh P.T. et al., 2019, ALMA observations of the circumstellar envelope around EP Aqr, *Research in Astronomy and Astrophysics*, 19, 043
- Nhung P. T., Hoai D. T., Tuan-Anh P. et al., 2021, Morphokinematics of the circumstellar envelope of the AGB star R Dor: a global view, *MNRAS*, 504, 2687
- Norris B. R. M., et al., 2012, A close halo of large transparent grains around extreme red giant stars, *Nature*, 484, 220
- Ohnaka K., Weigelt G., Hofmann K. H., 2016, Clumpy dust clouds and extended atmosphere of the AGB star W Hydrae revealed with VLT/SPHERE-ZIMPOL and VLTI/AMBER, *A&A*, 589, A91
- Ohnaka K., Weigelt G., Hofmann K. H., 2017, General catalogue of variable stars: Version GCVS 5.1, *A&A*, 597, A20
- Samus' N. N., Kazarovets E. V., Durlevich O. V. et al., 2017, General catalogue of variable stars: Version GCVS 5.1, *Astronomy Reports*, 61, 80
- Takigawa A., Kamizuka T., Tachibana S., Yamamura I., 2017, Dust formation and wind acceleration around the aluminum oxide-rich AGB star W Hydrae, *Science Advances*, 3, eaao2149
- Takigawa A., Kim T.-H., Igami Y. et al., 2019, Formation of Transition Alumina Dust around Asymptotic Giant Branch Stars: Condensation Experiments using Induction Thermal Plasma Systems, *ApJ*, 878, L7
- Vlemmings W., et al., 2017, The shock-heated atmosphere of an asymptotic giant branch star resolved by ALMA, *Nature Astronomy*, 1, 848
- Vlemmings W. H. T., et al., 2018, Rotation of the asymptotic giant branch star R Doradus, *A&A*, 613, L4
- Vlemmings W. H. T., Khouri T., Olofsson H., 2019, Resolving the extended stellar atmospheres of asymptotic giant branch stars at (sub)millimetre wavelengths, *A&A*, 626, A81
- Vlemmings W. H. T., Khouri T. and Tafoya D., 2021, Maser emission from the CO envelope of the asymptotic giant branch star W Hydrae, *A&A*, 654, A18
- Winters J. M., et al., 2021, Molecules, shocks, and disk in the axi-symmetric wind of the MS-type AGB star RS Cancri, *A&A*, submitted
- Zhao-Geisler R., Köhler R., Kemper F., et al., 2015, Spectro-Imaging of the Asymmetric Inner Molecular and Dust Shell Region of the Mira Variable W Hya with MIDI/VLTI, *PASP*, 127, 732
- van Leeuwen F., 2007, Validation of the new Hipparcos reduction, *A&A*, 474, 653